Defects Enhance Stability in 12-fold Symmetric Soft-Matter Quasicrystals

Alptuğ Ulugöl, Robert Hardeman, Frank Smallenburg, Laura Filion

Defects Enhance Stability in 12-fold Symmetric Soft-Matter Quasicrystals

Alptuğ Ulugöl,[1,*] Robert J. Hardeman,[1] Frank Smallenburg,[2] and Laura Filion[1]

[1] *Soft Condensed Matter and Biophysics, Debye Institute for Nanomaterials Science, Utrecht University, Utrecht, Netherlands*
[2] *Université Paris-Saclay, CNRS, Laboratoire de Physique des Solides, 91405 Orsay, France*

(Dated: November 24, 2025)

Quasicrystals are materials that exhibit long-range order without translational periodicity. In soft matter, the most commonly observed quasicrystal has 12-fold symmetry and consists of tilings made out of squares and triangles. Intriguingly, both in experiments and simulations, these tilings nearly always appear with many point defects. These defects can be decomposed into squares, triangles and an additional tile: a rhombus. In this letter, we explore how rhombus tiles change the entropy of square-triangle 12-fold quasicrystals. We introduce a novel lattice-based Monte Carlo simulation method that uses open boundaries to allow the concentration of different tile types to fluctuate. Our simulations show that rhombus tiles significantly increase the configurational entropy of the quasicrystal phase, enhancing its stability. These findings highlight the critical role of defects in stabilizing soft-matter quasicrystals.

Quasicrystals are exotic materials that possess long-range order despite lacking translational periodicity. Although originally discovered in metallic alloys [1], recent years have also seen the discovery of quasicrystals in a variety of soft-matter systems, from nanoparticles to granular matter [2–12]. Arguably the most common quasicrystal observed in soft matter is a two-dimensional quasicrystal with a 12-fold symmetry, which can be decomposed into a tiling consisting of squares and triangles [2, 13–15]. Intriguingly, in both experiments and simulations where these phases form spontaneously, the resulting tilings always contain a high concentration of point defects [7, 9, 11, 16–28]. Unlike point defects in regular crystals, which typically take the form of vacancies, interstitials, or antisite defects, these quasicrystal defects appear as the introduction of new tile shapes into the tiling. In the case of square-triangle tilings, these defect tiles manifest as shield-like or egg-like defects [7, 19, 20, 22, 26–28], each of which can be decomposed into squares, triangles, and an additional rhombus-shaped tile, as illustrated in Figure 1(a). The high prevalence of these defects suggests that they play an important role in the stability of soft-matter quasicrystals. Moreover, the diffusion of defect tiles through a square-triangle tiling has the side-effect of rearranging the underlying tiling pattern, hence providing a mechanism for the quasicrystal to sample the myriad of possible random tiling realizations [13]. Therefore, to understand the thermodynamic stability of soft-matter quasicrystals, we require an understanding of how these rhombus-shaped defects affect the entropy of square-triangle tilings.

In this Letter, we use a novel tile-based simulation approach combined with free-energy calculations to explore the effect of rhombus-shaped defects on the configurational entropy of the dodecagonal square-triangle tiling. In particular, we simulate systems with open boundary conditions. In contrast to periodic boundaries, open boundaries allow for fluctuations in the number, type and orientation of all tile types, as well as fluctuations in the global phason strain. This allows our simulations to sample the equilibrium tiling structure independent of the phase of the initial configuration. Using thermodynamic integration, we map out the free-energy landscape as a function of this biasing potential, and use the results to extract the entropy as a function of defect tile concentration. We show that in comparison to point defects in traditional crystals, defects in quasicrystal tilings provide a larger entropy gain, explaining the high concentration of defects observed in a variety of soft-matter quasicrystals.

Simulation methods have been developed to investigate quasicrystals on a lattice, but they present two major limitations for our purposes. First, they employ periodic boundary conditions and rely on periodic approximants of the quasicrystal. This approach inherently disrupts the aperiodicity of quasicrystals, which can alter the defect concentration, making it difficult to infer the true equilibrium defect concentration in the thermodynamic limit. Second, existing methods are based on intricate Monte Carlo (MC) moves, such as zipper moves[13], which maintain the number of different tiles. However, proving their detailed balance is typically done on a case-by-case basis. Extending these moves to include new tile types and allowing for type fluctuations without violating detailed balance is complex and often impractical. Therefore, these methods are not ideal for our study, which focuses on the equilibrium concentrations of different tiles (or defects).

To address these issues, we introduce a novel simulation method to explore lattice models under open boundary conditions (OBCs) with a new set of Monte Carlo (MC) moves, detailed in the Supplemental Material [29]. Our MC moves come in two types and can be adapted to any tiling. The first is a local vertex move, where a vertex rotates around a neighbor by $\pi/6$, corresponding to 12-fold symmetry. The second is a swap move, where pentagonal patches—tiled either with a square and a triangle or two rhombi and a triangle—are swapped. To

adapt these moves to other tilings, one simply adjusts the rotation angle to match the tiling's symmetry and identifies a patch with multiple tiling configurations for the swap move.

We implement OBCs in our model by incorporating a confining line tension, denoted by γ, which contributes to the potential energy as:

$$U_{\mathcal{B}} = \gamma L, \tag{1}$$

where L is the perimeter of the tiling. This energy contribution biases the system towards a simply-connected configuration, meaning the tilings consist of a single island without holes, while allowing the boundary shape to evolve to the most favorable configuration. By using OBCs, we simultaneously: (i) allow the quasicrystal's shape to fully relax and (ii) enable boundary fluctuations that facilitate the creation and annihilation of tiles. This allows the number of tiles of each type and orientation to fluctuate with a suitable set of MC moves, thereby overcoming the limitations of periodic boundary conditions.

To understand the defect statistics of square-triangle tilings using rhombus tiles as a proxy, we focus on the effect of rhombus tiles on the entropy of the tiling. To control the number of rhombi in our system, we introduce a chemical potential-like energy contribution:

$$U_{\mathcal{R}} = \epsilon_R n_R, \tag{2}$$

where ϵ_R is the energy cost of adding a rhombus and n_R is the number of rhombi. This biasing potential allows us to explore different tile compositions by varying ϵ_R. The total energy U is then simply the sum of Eqs. 1 and 2. Using this potential, we simulate square-triangle-rhombus tilings with biasing potentials $\beta\epsilon_R \in [-1, 7]$, line tensions $\beta\gamma a \in \{3, 4, 5, 6\}$, and the number of vertices $N \in \{996, 2121, 4123, 8004\}$. Here, $\beta = 1/k_B T$ with k_B Boltzmann's constant and T the temperature, and a is the length of an edge. We initialize the simulations with random inflationary Stampfli square-triangle tilings of type $[D, I]$ where D represents the size of the initial square lattice and I is the number of inflations performed on that square lattice [13]. We measure the boundary length, the number of different tiles, and the edge and tile orientations of various realizations of the square-triangle-rhombus tiling. A typical realization is depicted in Figure 1(b).

As a first step, we explore the orientational ordering of tiles and edges in our simulations. To achieve this, we calculate the Fourier transform (2D structure factor) of the vertices in our equilibrated patterns. As shown in Fig. 2(a-d), we observe clear 12-fold symmetry across a range of biasing parameters ϵ_R. This suggests that the tilings in our simulations remain in the quasicrystal phase. As a second check of our simulations, we confirmed that our patches of tiling remain compact (non-fractal) for the range of line tensions explored. As shown in the SM [29],

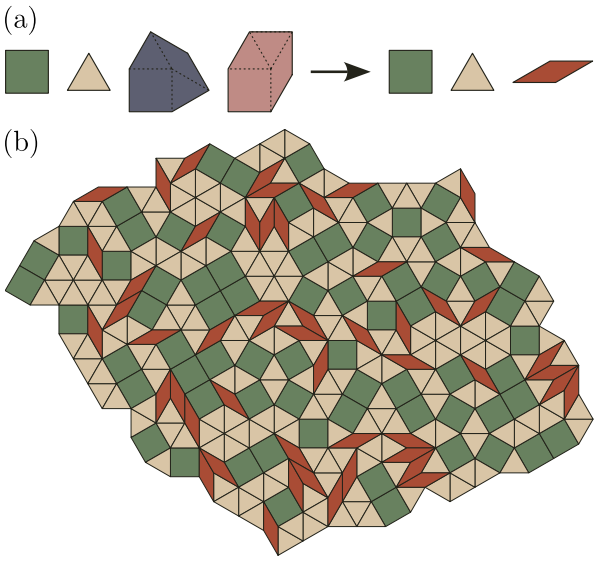

FIG. 1. (a) The tiles and point defects in 12-fold symmetric soft-matter quasicrystals. On the left-hand side, we depict the square, triangle, shield, and egg tiles, in order, with the latter two being the point defects. The dashed lines within the point defects show their decomposition into a square, two triangles, and an additional rhombus-shaped tile. On the right-hand side, we depict our simplified model tiles using the rhombus-shaped tile as the point defect representative. (b) A sample snapshot from the open boundary simulation of a square-triangle-rhombus tiling consisting of 256 vertices.

the average length of the perimeter scales with the square root of the number of particles, confirming that in the thermodynamic limit, the boundary becomes negligible.

We now explore the behavior of the concentration of different tile types as a function of the biasing strength ϵ_R which tunes the propensity of the system to include rhombi. Specifically, in Fig. 2 (e), we plot the fraction of the total area covered by squares, triangles, and rhombi as a function of ϵ_R. We find that for the values of $\beta\epsilon_R > -0.7$, the area fraction of triangles remains fixed at 1/2 within our error bars. This is consistent with what we would theoretically expect for a globally uniform 12-fold symmetric tiling[13–15], as also derived in the SM [29]. This result is essentially independent of the biasing potential and system size, and provides clear evidence that our simulations are correctly sampling the space of square-triangle-rhombus tilings.

In contrast, for the values of $\beta\epsilon_R < -0.7$, we observe that the area fraction of triangles starts deviating from 1/2. This suggests that either the global uniformity of the system or its 12-fold symmetry is disrupted, both of which may be attributable to a phase transition to a more rhombus-heavy phase. As this Letter is focused on the 12-fold symmetric phase, we do not explore this transition in more detail.

In the 12-fold symmetric regime, the concentration of rhombi goes down continuously as ϵ_R increases, with the

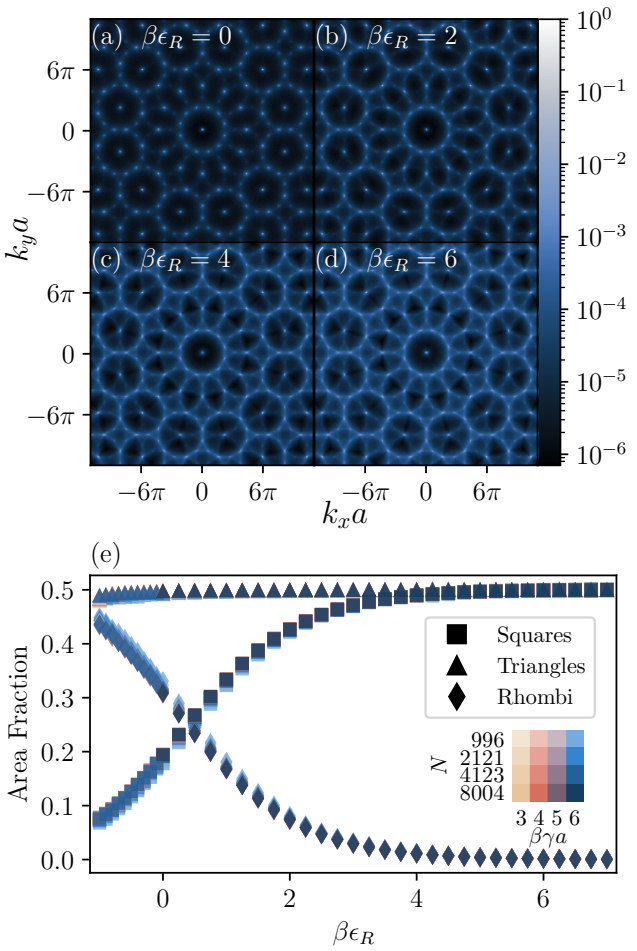

FIG. 2. Ensemble averaged 2D structure factors of the tilings at $N = 8004$, $\beta\gamma a = 4$, $\beta\epsilon_R =$ (a) 0, (b) 2, (c) 4, and (d) 6. structure factors of single snapshots can be found in SM [29]. (e) The area fractions of the tiles as a function of the rhombus biasing potential. The number of vertices and the line tension is color-coded as shown in the panel.

concentration of squares trivially increasing correspondingly (as the three area fractions must necessarily add up to 1). For sufficiently large $\epsilon_R \gtrsim 6$, the number of rhombi becomes vanishingly small in comparison to the total system size, bringing us essentially to the pure square-triangle limit.

The key question that we would like to answer next is how much the rhombi add to the total entropy of the system. In other words, we are interested in the entropy difference

$$\Delta S(N, \gamma, T, \epsilon_R) = S(N, \gamma, T, \epsilon_R) - S_{\mathrm{sq-tr}}(N, \gamma, T), \quad (3)$$

where S is the entropy of a tiling containing a finite concentration of rhombi (controlled by ϵ_R), and $S_{\mathrm{sq-tr}}$ is the entropy of a square triangle tiling without rhombi (which occurs when $\epsilon_R \to \infty$). Note that in the thermodynamic limit ($N \to \infty$), we expect the effects of the boundary to become negligible, and hence

$$\Delta S = N \Delta s(\beta\epsilon_R), \quad (4)$$

with Δs the entropy difference per particle between a pure square-triangle tiling and our square-triangle-rhombus tiling. To calculate ΔS, it is convenient to first calculate the Helmholtz free-energy difference ΔF, which is related to the entropy difference via $\Delta F = \Delta U - T\Delta S$. Here, ΔU is the potential energy difference between a system at finite ϵ_R and a square-triangle tiling at $\epsilon_R \to \infty$, which is given by:

$$\Delta U(N, \gamma, T, \epsilon_R) = \epsilon_R \langle n_R \rangle_{N,\gamma,T,\epsilon_R} + \gamma \left(\langle L \rangle_{N,\gamma,T,\epsilon_R} - \langle L \rangle_{N,\gamma,T,\infty} \right). \quad (5)$$

Using thermodynamic integration, ΔF can be calculated from the data in Fig. 2(e) via

$$\begin{aligned} \Delta F(N, \gamma, T; \epsilon_R) &= \int_{\epsilon_R}^{\infty} \mathrm{d}\epsilon'_R \left\langle \frac{\partial U}{\partial \epsilon_R} \right\rangle_{N,\gamma,T,\epsilon'_R}, \\ &= \int_{\epsilon_R}^{\infty} \mathrm{d}\epsilon'_R \langle n_R \rangle_{N,\gamma,T,\epsilon'_R}, \end{aligned} \quad (6)$$

where $\langle \ldots \rangle$ represents an ensemble average.

Note that if we want to calculate the total entropy of our system, we have to combine ΔS with the configurational entropy of the pure square-triangle tiling. For an infinitely large system this has been calculated exactly using the Bethe ansatz [30, 31], and is given by

$$\frac{S_{\mathrm{sq-tr}}}{N k_B} = \log(108) - 2\sqrt{3} \log\left(2 + \sqrt{3}\right) = 0.12005524\ldots \quad (7)$$

From ΔU and ΔF, we calculate the configurational entropy of our tilings as a function of ϵ_R, and plot the results in Figure 3(a). Note that we have included here the base entropy of the square triangle tiling (dashed line), using the infinite-system value. First of all, we indeed find that for large systems, our results obtained at different γ converge. Additionally, we observe a substantial increase in the configurational entropy per vertex as the rhombus cost $\beta\epsilon_R$ decreases. Specifically, at the point where there is no rhombus cost ($\beta\epsilon_R = 0$), the rhombus area fraction approaches 0.306 ± 0.001 and the configurational entropy reaches a maximum. To investigate this point, we plot the finite-size scaling of the entropy of the square-triangle-rhombus tiling at $\epsilon_R = 0$ for different line tensions in Fig. 3(b). When we fit a line through the larger system sizes (indicated by filled markers) for line tensions $\beta\gamma a = 4, 5, 6$, we observe that all systems converge well at the infinite system size limit ($1/N = 0$). Comparing the different line tensions, we observe that the $\beta\gamma a = 3$ case produces the largest deviation, likely because the boundary fluctuations are more prominent for low γ. Hence, it is excluded from the infinite system extrapolation to get an unbiased estimate.

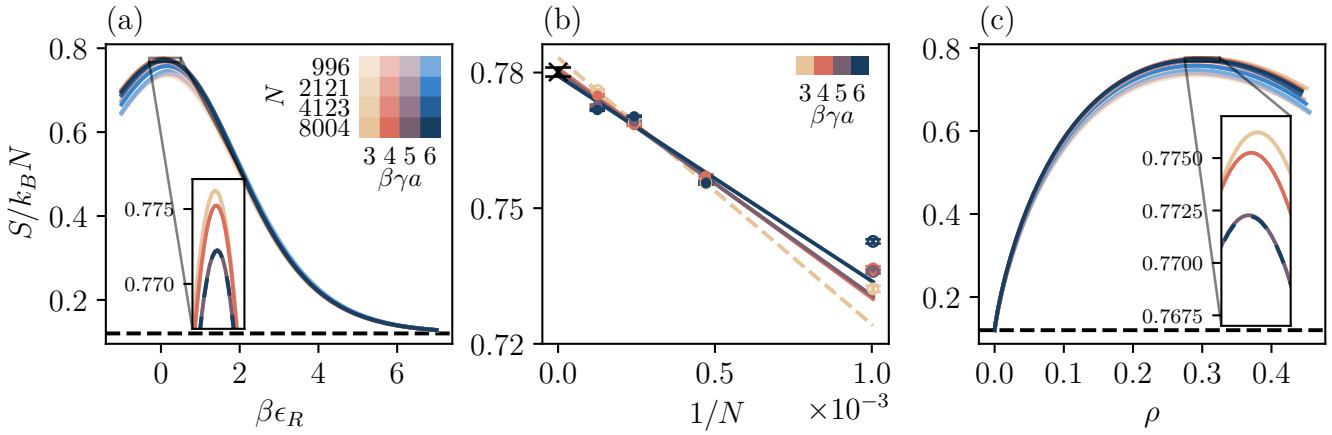

FIG. 3. Configurational entropy per vertex with respect to varying (a) rhombus biasing potential, (b) system sizes (at $\beta\epsilon_R = 0$) and (c) rhombus area fraction. In panels (a) and (c), black dashed lines indicate the configurational entropy of square-triangle tiling and the markers indicate the maximally random square-triangle-rhombus tiling, and the insets zoom in to the entropy peak of the largest system size ($\beta\gamma a = 6$ is drawn using dashed lines to increase visibility) . In panel (b), lines indicate linear fits to the data where the smallest system size ($N = 996$) is excluded. The $\times$ marker at $1/N = 0$ shows the entropy at infinite system extrapolation obtained from the solid lines ($\beta\gamma a = 4, 5, 6$), which is given by $S/k_BN = 0.780 \pm 0.001$. All error bars are set to three times the standard error. The number of vertices and the line tensions are color-coded as shown in the figure. The plots of individual curves in panels (a) and (b) can be found in the SM [29].

We find the configurational entropy of the infinite system as $0.780 \pm 0.001\, k_B$ per particle, which is approximately 6.5 times the configurational entropy of the pure square-triangle tiling.

While ϵ_R is a useful control parameter in our simulation model, in the context of comparing to observed quasicrystals in literature it is more intuitive to examine how the entropy increase due to rhombi is related to their concentration. To this end, we plot in Fig. 3(c) the same entropy data as in Fig. 3(a), but as a function of the rhombus area fraction ρ. We observe a sharp increase in entropy as soon as even a small concentration of rhombi is added to the tiling, with the entropy reaching a maximum (as expected) for the rhombus concentration corresponding to $\epsilon_R = 0$.

The sharp increase at the start of the plot in Fig. 3(c) is interesting in the context of rhombic defects in otherwise pure square-triangle tilings. In particular, it is interesting to determine the amount of entropy added by a single rhombus defect to the tiling. To put this in context, adding a single point defect (vacancy or interstitial) to a normal crystal would, in the thermodynamic limit, add a total entropy of $S_1 = \log M$ to the system, where M is the number of available lattice sites for the defect (for a vacancy, M is generally just the number of particles). We can calculate the entropy gain of adding a single rhombus tile to an otherwise pure square-triangle tiling, by looking at the behavior of the number of rhombi as a function of ϵ_R in the limit of nearly pure square-triangle tilings. When the concentration of rhombi is sufficiently low, such that they do not interact, the number of rhombi will scale as

$$n_R = e^{-\beta\epsilon_R + \Delta S_1/k_B}, \tag{8}$$

where ΔS_1 is now the configurational entropy added by creating a single rhombus. Note that extensivity of the number of rhombi implies that ΔS_1 must of the form $\Delta S_1/k_B = c + \log N$, with c a constant. In Fig. 4, we plot the defect concentration n_R/N as a function of ϵ_R on a logarithmic scale, and fit the high-ϵ_R regime to obtain the constant c. Extrapolating to infinite system sizes, we obtain $\Delta S_1/k_B = 0.056(4) + \log N$, which is considerably higher than the $\log N$ we would expect for a simple vacancy in a crystal. Recall that the entropy gain of adding an extra vertex to the tiling is approximately $0.12k_B$ [30, 31]. Hence, in comparison to adding a vacancy, including a rhombus defect adds nearly half as much configurational entropy as one would gain when adding an extra particle to the system. Moreover, by considering that any configuration containing a rhombus tile can be mapped to a configuration containing either a shield or an egg tile, it is possible to predict that for shield and egg defects, the combined entropy for including a single defect is of the same order of magnitude, corresponding to $\Delta S_1^*/k_B \simeq 0.022 + \log N$ (see SM [29]). This significant boost in entropy even for a single defect provides an explanation for the prevalence of defects in virtually all square-triangle tilings observed in soft-matter systems [7, 9, 11, 20–28].

In practice, the entropy gain of creating a defect in a square-triangle must be compared to the free-energy cost associated with creating such a defect at a specific

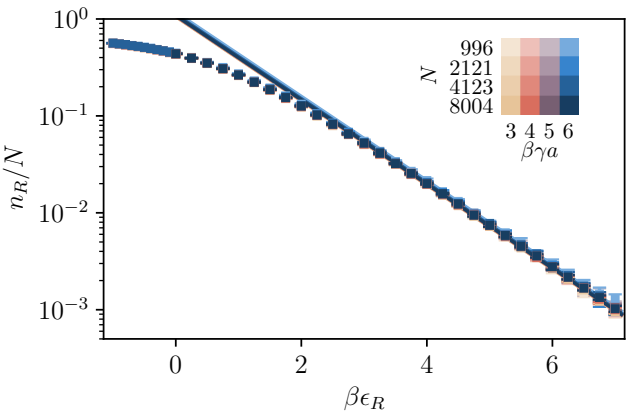

FIG. 4. The ensemble average of the number of rhombus with respect to varying rhombi biasing potential. The solid curves indicate exponentially decaying fits to the tails of the data. Error bars show three times the standard errors.

location. In our lattice model, this cost is zero, but for a system of interacting particles at finite pressure, there will always be a positive free-energy cost to creating a defect. We note, however, that in the case of the shield and egg defects typically found in square-triangle tilings, the shield and egg defects (which each incorporate one rhombus tile) are often the result of breaking up a vacancy into two separate defects. This implies that the volume cost – typically a key part of the cost of creating a defect – of creating shield and egg tiles, is only half of that of a full vacancy. Hence, the total free-energy cost of creating rhombus-containing defects in square-triangle tilings is low, which combined with the high entropy gain implies that high defect concentrations should be expected.

We note that in order to quantitatively predict equilibrium defect concentrations in an off-lattice model that forms square-triangle tilings, our predictions of the *configurational* entropy of defect formation need to be combined with a determination of the associated cost or gain in *vibrational* free energy, corresponding to ϵ_R in our model. Existing theoretical and simulation-based methods can be used to explore the vibrational free energy of quasicrystals, including density functional theory [32–35], phase field crystal theory [36, 37], Lifshitz-Petrich theory [38, 39], and the Frenkel-Ladd method [19, 40–43].

In conclusion, we introduce a novel simulation method designed to explore square-triangle-rhombus tilings under open boundary conditions by incorporating a confining line tension, and use it to analyze the configurational entropy gain associated with adding rhombi to a square-triangle quasicrystal. Our results show that rhombus defects are significantly more entropically favorable than conventional point defects in periodic crystals, explaining the observed prevalence of these defects in soft-matter quasicrystals. While we have focused here on the 12-fold square-triangle quasicrystal, we strongly expect that this result is general to the much broader set of thermodynamically stable random-tiling quasicrystals, due to the additional flexibility in tiling configurations offered by the introduction of an additional tile shape.

DATA AVAILABILITY

Codes and data associated with this letter are available in GitHub and Zenodo at the following repositories:
`https://github.com/alptug/12FoldQC-Sim`
`https://doi.org/10.5281/zenodo.14283005`

ACKNOWLEDGEMENTS

AU thanks Stefanie D. Pritzl for fruitful discussions. AU and LF acknowledge funding from the Dutch Research Council (NWO) under the grant number OCENW.GROOT.2019.071.

* a.ulugol@uu.nl

[1] D. Shechtman, I. Blech, D. Gratias, and J. W. Cahn, Metallic phase with long-range orientational order and no translational symmetry, Phys. Rev. Lett. **53**, 1951 (1984).
[2] E. Fayen, M. Impéror-Clerc, L. Filion, G. Foffi, and F. Smallenburg, Self-assembly of dodecagonal and octagonal quasicrystals in hard spheres on a plane, Soft Matter **19**, 2654 (2023).
[3] X. Zeng, G. Ungar, Y. Liu, V. Percec, A. E. Dulcey, and J. K. Hobbs, Supramolecular dendritic liquid quasicrystals, Nature **428**, 157 (2004).
[4] X. Zeng, B. Glettner, U. Baumeister, B. Chen, G. Ungar, F. Liu, and C. Tschierske, A columnar liquid quasicrystal with a honeycomb structure that consists of triangular, square and trapezoidal cells, Nat. Chem. **15**, 625 (2023).
[5] S. Förster, K. Meinel, R. Hammer, M. Trautmann, and W. Widdra, Quasicrystalline structure formation in a classical crystalline thin-film system, Nature **502**, 215 (2013).
[6] S. Förster, S. Schenk, E. Maria Zollner, O. Krahn, C.-T. Chiang, F. O. Schumann, A. Bayat, K.-M. Schindler, M. Trautmann, R. Hammer, *et al.*, Quasicrystals and their approximants in 2d ternary oxides, Phys. Status Solidi B **257**, 1900624 (2020).
[7] K. Hayashida, T. Dotera, A. Takano, and Y. Matsushita, Polymeric quasicrystal: mesoscopic quasicrystalline tiling in abc star polymers, Phys. Rev. Lett. **98**, 195502 (2007).
[8] X. Li, L. H. Chan, S.-i. Takakura, M. Nakatake, T. Yamada, R. Tamura, and J. Yuhara, Growth of a quasicrystal-related structure and superstructure for ultrathin Ce–Ti–O films on Pt (111), Phys. Chem. Chem. Phys. **25**, 26065 (2023).
[9] L. Liu, Z. Li, Y. Li, and C. Mao, Rational design and self-assembly of two-dimensional, dodecagonal dna quasicrystals, J. Am. Chem. Soc. **141**, 4248 (2019).

[10] J. I. Urgel, D. Ecija, G. Lyu, R. Zhang, C.-A. Palma, W. Auwaerter, N. Lin, and J. V. Barth, Quasicrystallinity expressed in two-dimensional coordination networks, Nat. Chem. **8**, 657 (2016).

[11] S. Schenk, O. Krahn, E. Cockayne, H. L. Meyerheim, M. de Boissieu, S. Förster, and W. Widdra, 2d honeycomb transformation into dodecagonal quasicrystals driven by electrostatic forces, Nat. Commun. **13**, 7542 (2022).

[12] A. Plati, R. Maire, E. Fayen, F. Boulogne, F. Restagno, F. Smallenburg, and G. Foffi, Quasi-crystalline order in vibrating granular matter, Nat. Phys. **20**, 465 (2024).

[13] M. Oxborrow and C. L. Henley, Random square-triangle tilings: A model for twelvefold-symmetric quasicrystals, Phys. Rev. B **48**, 6966 (1993).

[14] M. Impéror-Clerc, A. Jagannathan, P. Kalugin, and J.-F. Sadoc, Square-triangle tilings: An infinite playground for soft matter, Soft Matter **17**, 9560 (2021).

[15] M. Impéror-Clerc, P. Kalugin, S. Schenk, W. Widdra, and S. Förster, Higher-dimensional geometrical approach for the characterization of two-dimensional square-triangle-rhombus tilings, Phys. Rev. B **110**, 144106 (2024).

[16] X. Ye, J. Chen, M. Eric Irrgang, M. Engel, A. Dong, S. C. Glotzer, and C. B. Murray, Quasicrystalline nanocrystal superlattice with partial matching rules, Nat. Mater. **16**, 214 (2017).

[17] S. Rochal, O. Konevtsova, I. Shevchenko, and V. Lorman, Soft spherical nanostructures with a dodecagonal quasicrystal-like order, Soft Matter **12**, 1238 (2016).

[18] Y. Liu, T. Liu, X.-Y. Yan, Q.-Y. Guo, H. Lei, Z. Huang, R. Zhang, Y. Wang, J. Wang, F. Liu, *et al.*, Expanding quasiperiodicity in soft matter: Supramolecular decagonal quasicrystals by binary giant molecule blends, Proc. Natl. Acad. Sci. U.S.A. **119**, e2115304119 (2022).

[19] C. R. Iacovella, A. S. Keys, and S. C. Glotzer, Self-assembly of soft-matter quasicrystals and their approximants, Proc. Natl. Acad. Sci. U.S.A. **108**, 20935 (2011).

[20] T. Dotera, T. Oshiro, and P. Ziherl, Mosaic two-lengthscale quasicrystals, Nature **506**, 208 (2014).

[21] R. Ryltsev and N. Chtchelkatchev, Universal self-assembly of one-component three-dimensional dodecagonal quasicrystals, Soft Matter **13**, 5076 (2017).

[22] M. N. van der Linden, J. P. Doye, and A. A. Louis, Formation of dodecagonal quasicrystals in two-dimensional systems of patchy particles, J. Chem. Phys. **136**, 054904 (2012).

[23] D. F. Tracey, E. G. Noya, and J. P. Doye, Programming patchy particles to form three-dimensional dodecagonal quasicrystals, J. Chem. Phys. **154**, 194505 (2021).

[24] T. Ishimasa, H.-U. Nissen, and Y. Fukano, Electron microscopy of crystalloid structure in Ni-Cr small particles, Philos. Mag. A **58**, 835 (1988).

[25] M. Dzugutov, Formation of a dodecagonal quasicrystalline phase in a simple monatomic liquid, Phys. Rev. Lett. **70**, 2924 (1993).

[26] S. Schenk, E. M. Zollner, O. Krahn, B. Schreck, R. Hammer, S. Förster, and W. Widdra, Full real-space analysis of a dodecagonal quasicrystal, Acta Cryst. A **75**, 307 (2019).

[27] N. P. Kryuchkov, S. O. Yurchenko, Y. D. Fomin, E. N. Tsiok, and V. N. Ryzhov, Complex crystalline structures in a two-dimensional core-softened system, Soft Matter **14**, 2152 (2018).

[28] D. V. Talapin, E. V. Shevchenko, M. I. Bodnarchuk, X. Ye, J. Chen, and C. B. Murray, Quasicrystalline order in self-assembled binary nanoparticle superlattices, Nature **461**, 964 (2009).

[29] See Supplemental Material at URL-will-be-inserted-by-publisher for the detailed explanations of geometric constraints, methodological details, extended plots, and the mapping of rhombi into shields and eggs.

[30] M. Widom, Bethe ansatz solution of the square-triangle random tiling model, Phys. Rev. Lett. **70**, 2094 (1993).

[31] P. Kalugin, The square-triangle random-tiling model in the thermodynamic limit, J. Phys. A Math. Gen. **27**, 3599 (1994).

[32] A. J. Archer, T. Dotera, and A. M. Rucklidge, Rectangle-triangle soft-matter quasicrystals with hexagonal symmetry, Phys. Rev. E **106**, 044602 (2022).

[33] A. Scacchi, W. R. C. Somerville, D. M. A. Buzza, and A. J. Archer, Quasicrystal formation in binary soft matter mixtures, Phys. Rev. Res. **2**, 032043 (2020).

[34] P. Subramanian, D. J. Ratliff, A. M. Rucklidge, and A. J. Archer, Density distribution in soft matter crystals and quasicrystals, Phys. Rev. Lett. **126**, 218003 (2021).

[35] D. J. Ratliff, A. J. Archer, P. Subramanian, and A. M. Rucklidge, Which wave numbers determine the thermodynamic stability of soft matter quasicrystals?, Phys. Rev. Lett. **123**, 148004 (2019).

[36] C. V. Achim, M. Schmiedeberg, and H. Löwen, Growth modes of quasicrystals, Phys. Rev. Lett. **112**, 255501 (2014).

[37] P. Subramanian, A. J. Archer, E. Knobloch, and A. M. Rucklidge, Spatially localized quasicrystalline structures, New J. Phys. **20**, 122002 (2018).

[38] R. Lifshitz and H. Diamant, Soft quasicrystals–why are they stable?, Phil. Mag. **87**, 3021 (2007).

[39] K. Jiang, J. Tong, P. Zhang, and A.-C. Shi, Stability of two-dimensional soft quasicrystals in systems with two length scales, Phys. Rev. E **92**, 042159 (2015).

[40] E. Fayen, L. Filion, G. Foffi, and F. Smallenburg, Quasicrystal of binary hard spheres on a plane stabilized by configurational entropy, Phys. Rev. Lett. **132**, 048202 (2024).

[41] M. Engel, Entropic stabilization of tunable planar modulated superstructures, Phys. Rev. Lett. **106**, 095504 (2011).

[42] A. Kiselev, M. Engel, and H.-R. Trebin, Confirmation of the random tiling hypothesis for a decagonal quasicrystal, Phys. Rev. Lett. **109**, 225502 (2012).

[43] H. Pattabhiraman, A. P. Gantapara, and M. Dijkstra, On the stability of a quasicrystal and its crystalline approximant in a system of hard disks with a soft corona, J. Chem. Phys. **143**, 164905 (2015).

Supplemental Material: Defects Enhance Stability in 12-fold Symmetric Soft-Matter Quasicrystals

Alptuğ Ulugöl,[1,*] Robert J. Hardeman,[1] Frank Smallenburg,[2] and Laura Filion[1]

[1] *Soft Condensed Matter and Biophysics, Debye Institute of Nanomaterials Science, Utrecht University, Utrecht, Netherlands*
[2] *Université Paris-Saclay, CNRS, Laboratoire de Physique des Solides, 91405 Orsay, France*

(Dated: November 24, 2025)

CONTENTS

I. Constraints on the distribution of tiles 1
A. Constraint 1: Simply-connected tiling 1
B. Constraint 2: Global uniformity 1
C. Constraint 3: Rotational symmetry 2

II. Methodological Details 3
A. Open Boundaries and Tile Biasing 3
B. Markov-Chain Monte Carlo Simulation 3
1. Vertex Moves 3
2. Swap Moves 4
C. Configurational Entropy Calculation 5

III. 2D Structure Factors of Single Snapshots 7

IV. Alternative Representation of the Plots from Figure 2 a & c from the Main Text 7

V. Mapping Rhombi into Shields and Eggs 7

References 9

I. CONSTRAINTS ON THE DISTRIBUTION OF TILES

Here, we investigate the theoretical constraints on the tile compositions of 12-fold symmetric square-triangle-rhombus tilings in the thermodynamic limit. To this end, we follow the approach of Refs. [1–3]. We consider a large patch of tiling, consisting entirely of squares, equilateral triangles, and rhombi, all with identical edge lengths. Such a tiling can be described by its area fractions of squares, triangles, and rhombi of different orientations. In particular, we denote the total area fractions of each type of tile as

$$\sigma = \sum_{i=1}^{3} \sigma_i, \quad \tau = \sum_{i=1}^{4} \tau_i, \quad \rho = \sum_{i=1}^{6} \rho_i, \tag{S1}$$

with the subscripted area fractions σ_i, τ_i, and ρ_i denoting the fraction of patch area covered by squares, triangles, and rhombi of orientation i, respectively. We denote a square of orientation i as an S_i square, and similarly T_i and R_i for triangles, and rhombi. Illustrations of each of the tile orientations can be seen in Table S1. In total, this corresponds to 13 degrees of freedom. In the following, we derive constraints on this set of parameters in order to make predictions about the tile concentrations for general random square-triangle-rhombus tilings.

A. Constraint 1: Simply-connected tiling

The first assumption we make about our tiling that it is free of holes and overlaps. In other words, there are no tile shapes other than squares, triangles, or rhombi, and that all space enclosed by the perimeter of the tiling is covered by exactly one tile. This leads to our first constraint on the tile concentration:

$$\sigma + \tau + \rho = 1, \tag{S2}$$

which simply states that all of space must be covered by tiles.

B. Constraint 2: Global uniformity

The second assumption we make about our patch of tiling is that it is globally uniform: if we take a large enough sub-patch of the tiling, it should have approximately the same tile concentrations as the overall patch, regardless of the location of the sub-patch.

As shown in Ref. [1], the global uniformity condition gives rise to the following constraint:

$$\det \langle B \rangle = \langle \det B \rangle , \tag{S3}$$

where B is the hyperslope of the mapping from the parallel-space to the perpendicular-space representation of the tiling. The hyperslopes of the individual tiles are given in Table S1 (see also Ref. [3]).

For the square-triangle-rhombus tilings, the average hyperslope-determinant is given by

$$\begin{aligned} \langle \det B \rangle &= \sum_{i=1}^{3} \sigma_i \det B_{S_i} + \sum_{i=1}^{4} \tau_i \det B_{T_i} + \sum_{i=1}^{6} \rho_i \det B_{R_i} \\ &= -\sum_{i=1}^{3} \sigma_i + \sum_{i=1}^{4} \tau_i - \sum_{i=1}^{6} \rho_i \\ &= \tau - (\sigma + \rho). \end{aligned} \tag{S4}$$

* a.ulugol@uu.nl

Similarly, the determinant of the average hyperslope is given by

$$\begin{aligned}\det\langle B\rangle = 12(&\rho_1\rho_3 - \rho_1\rho_4 + \rho_1\rho_5 + \rho_2\rho_4\\ &- \rho_2\rho_5 + \rho_2\rho_6 + \rho_4\rho_6 + \rho_3\rho_5 - \rho_3\rho_6)\\ &+ 6(\rho_1\sigma_3 + \rho_2\sigma_1 + \rho_3\sigma_2 + \rho_4\sigma_3 + \rho_5\sigma_1 + \rho_6\sigma_2)\\ &- 4(\tau_1\tau_2 + \tau_2\tau_3 + \tau_3\tau_4 + \tau_4\tau_1)\\ &+ 3(\sigma_1\sigma_2 + \sigma_2\sigma_3 + \sigma_3\sigma_1)\\ &+ \tau^2 - (\sigma+\rho)^2.\end{aligned} \tag{S5}$$

C. Constraint 3: Rotational symmetry

Finally, in order to restrict ourselves to quasicrystalline tilings with 12-fold symmetry, we impose that for each tile, all orientations occur equally frequently:

$$\sigma_i = \frac{\sigma}{4}, \quad \tau_i = \frac{\tau}{3}, \quad \rho_i = \frac{\rho}{6}. \tag{S6}$$

As a result of this, the right-hand side of Eq. S5 vanishes, and hence Eq. S3 reduces to:

$$\tau - (\sigma + \rho) = 0. \tag{S7}$$

Finally, combining equations (S2) and (S7) yields the theoretical constraints on the area fractions [3]:

$$\tau = \frac{1}{2}, \quad \sigma + \rho = \frac{1}{2}. \tag{S8}$$

X_i	Tile	Area	B_{X_i}	$\det B_{X_i}$
S_1	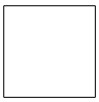	a^2	$\begin{pmatrix}1 & 0\\ 0 & -1\end{pmatrix}$	-1
S_2	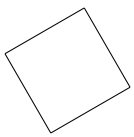	a^2	$\begin{pmatrix}-1/2 & -\sqrt{3}/2\\ -\sqrt{3}/2 & 1/2\end{pmatrix}$	-1
S_3	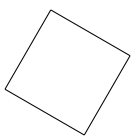	a^2	$\begin{pmatrix}-1/2 & \sqrt{3}/2\\ \sqrt{3}/2 & 1/2\end{pmatrix}$	-1
T_1		$\frac{\sqrt{3}}{4}a^2$	$\begin{pmatrix}1 & 0\\ 0 & 1\end{pmatrix}$	1
T_2	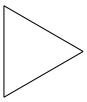	$\frac{\sqrt{3}}{4}a^2$	$\begin{pmatrix}-1 & 0\\ 0 & -1\end{pmatrix}$	1
T_3		$\frac{\sqrt{3}}{4}a^2$	$\begin{pmatrix}1 & 0\\ 0 & 1\end{pmatrix}$	1
T_4	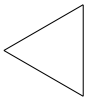	$\frac{\sqrt{3}}{4}a^2$	$\begin{pmatrix}-1 & 0\\ 0 & -1\end{pmatrix}$	1
R_1	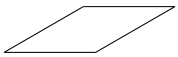	$\frac{1}{2}a^2$	$\begin{pmatrix}1 & -2\sqrt{3}\\ 0 & -1\end{pmatrix}$	-1
R_2	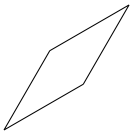	$\frac{1}{2}a^2$	$\begin{pmatrix}-2 & \sqrt{3}\\ -\sqrt{3} & 2\end{pmatrix}$	-1
R_3		$\frac{1}{2}a^2$	$\begin{pmatrix}1 & 0\\ 2\sqrt{3} & -1\end{pmatrix}$	-1
R_4		$\frac{1}{2}a^2$	$\begin{pmatrix}1 & 0\\ -2\sqrt{3} & -1\end{pmatrix}$	-1
R_5	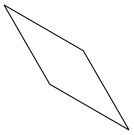	$\frac{1}{2}a^2$	$\begin{pmatrix}-2 & -\sqrt{3}\\ \sqrt{3} & 2\end{pmatrix}$	-1
R_6	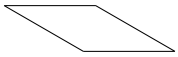	$\frac{1}{2}a^2$	$\begin{pmatrix}1 & 2\sqrt{3}\\ 0 & -1\end{pmatrix}$	-1

TABLE S1: The properties of the different tile orientations encountered in a square-triangle-rhombus tiling. The areas are given for edges of length a. The hyperslopes are the Jacobian matrices of the mapping of vertices between parallel and perpendicular space.

II. METHODOLOGICAL DETAILS

In this section we introduce the details of the open boundary simulations and describe the analysis methods for the square-triangle-rhombus tilings. We start by describing our model, in particular, how the open boundaries and tile biasing are introduced. Then, we describe how the initial square-triangle tiling is generated. Next, we introduce the vertex and swap moves for the Monte Carlo simulation. Finally, we explain how the simulation data is analysed, i.e., how the unbiasing and thermodynamic integration is performed to obtain the configurational entropy of square-triangle-rhombus tiling.

A. Open Boundaries and Tile Biasing

Putting quasicrystals into a periodic simulation box necessarily breaks the inherent aperiodicity of the quasicrystal, making it difficult to unravel in simulations whether defects appear due to kinetic trapping or their influence on the free energy of the system. In an effort to address this, we introduce a new simulation method designed to explore square-triangle-rhombus tilings under open boundary conditions by incorporating a confining line tension, denoted by γ. Specifically, in our simulations we consider a single patch of square-triangle-rhombus tiling on a quascrystalline lattice, and include a boundary contribution to the potential energy, given by

$$U_{\mathcal{B}} = \gamma L, \tag{S9}$$

where L denotes the circumference of the tiling. This contribution biases the system towards compact configurations while letting the tiling evolve to most favorable boundary shape for a given value of γ. Note that in the thermodynamic limit ($N \to \infty$), the effects of the boundary are expected to vanish and hence in this limit our results should become independent of our choice of γ.

To control the tile composition of the system, we introduce a chemical potential-like energy contribution for every tile type,

$$U_{\mathcal{T}} = \sum_{t \in \mathcal{T}} \epsilon_t n_t, \tag{S10}$$

where ϵ_t, n_t are the energy contribution and the number of tile type t. The set of tile types is defined as $\mathcal{T} = \{S, T, R\}$ representing squares, triangles and rhombi

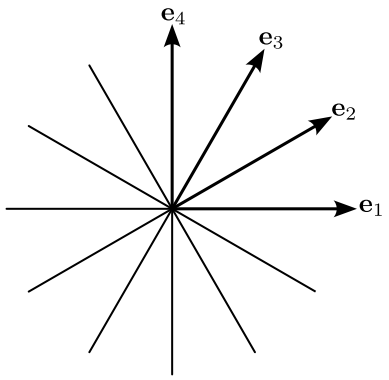

FIG. S1. Possible connected neighbor positions of a vertex.

respectively. Using this biasing potential, we can explore the free energies of different tile compositions by changing the energy contribution of each tile type. For the purpose of this paper we focus on systems where $\epsilon_S = \epsilon_T = 0$, and hence only vary ϵ_R.

With both energy contributions, Eqs.(S9,S10), combined, we arrive at the total energy that we use to simulate the system,

$$U = U_{\mathcal{B}} + U_{\mathcal{T}} = \gamma L + \epsilon_R n_R. \tag{S11}$$

Having established the model, we proceed with the introduction of the simulation details.

B. Markov-Chain Monte Carlo Simulation

Here we consider Markov Chain Monte Carlo (MCMC) simulations of tilings with a fixed number of vertices and let the number of squares, triangles, and rhombi fluctuate. We use two types of MC moves: (i) vertex moves and (ii) swap moves. The vertex moves enable local rearrangements of the tiling and the swap moves enable non-local transport of vertices. We provide the details of these moves in the following.

1. Vertex Moves

To construct a vertex move, first, we need to identify every possible position a vertex can have with respect to its neighbours. When we consider every orientation of the allowed tiles, we find that the relative position of two connected vertices can assume twelve possible vectors as shown in Figure (S1) where every subsequent vector is a $\pi/6$ rotation of the previous. Therefore we perform our simulation on a quasicrystalline lattice where each potential vertex location is connected to 12 others. One way to construct a vertex move is to choose a pair of existing connected vertices and rotate one of the vertices

around the other by an angle of $\pi/6$ clockwise or counter-clockwise. This type of vertex move enables tile propagation in the bulk and tile creation/annihilation at the boundary. However, this move should be implemented with care to allow only square, triangle, and rhombus tiles to exist and obey detailed balance. Our implementation of the vertex move consists of eight steps:

1. Choose a random vertex, i, in the tiling to displace.
2. Choose a random direction out of the 12 possible directions that a connected neighbor of vertex i could occupy.
3. If there is a vertex in the randomly chosen direction, identify it as the vertex j. Otherwise reject the move. Vertex j is the pivot of vertex i's rotation.
4. Choose a random rotation direction, i.e., clockwise or counter-clockwise. Rotate vertex i around vertex j by $\pi/6$ in the chosen direction.
5. If vertex i overlaps with another vertex, reject the move.
6. Check the tiles which are altered by vertex i's movement. If there is an invalid tile, i.e., a tile which is not a square, a triangle or a rhombus, reject the move. An example is depicted in Figure (S2)
7. Check if the tiling remains connected. If the tiling separated into multiple disconnected pieces, reject the move.
8. Accept the move with probability,

$$P_{\text{acc}}(i \to f) = \min\left(1, e^{-\beta(U_f - U_i)}\right), \tag{S12}$$

where $U_{i,f}$ are the potential energies of the initial and final state given by Eq. (S11). Note that $\beta = 1/k_B T$ is the inverse thermal energy.

Since this implementation of the vertex moves propagates the tiles in the bulk without changing the tile counts or the boundary length, valid bulk moves are always accepted. A sample vertex move in bulk is depicted in Figure S3(a). Moreover, the fluctuations on the boundary facilitate the creation and the annihilation of different tiles. Therefore, the dynamics of the MCMC algorithm can be summarized by (i) tile creation/annihilation at the boundary and (ii) propagation of tiles in the bulk. However, due to many validation steps in the algorithm, the majority of the proposed moves end up being invalid, resulting in relatively low acceptance rates.

2. *Swap Moves*

To improve the equilibration times we propose another type of move which we call a swap move. To construct

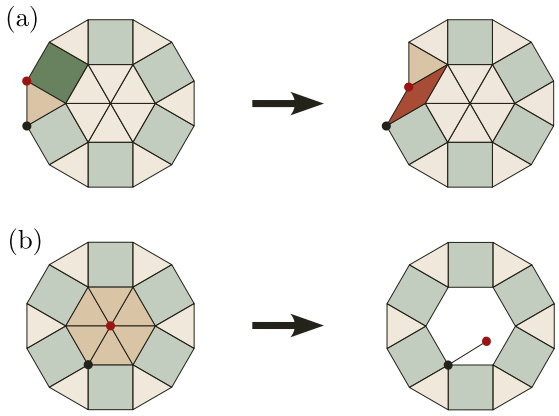

FIG. S2. The red vertex attempts to rotate clockwise around the blue vertex by an angle of $\pi/6$. (a) The move results in a valid tiling and may be accepted. (b) The move results in an invalid tiling and is rejected.

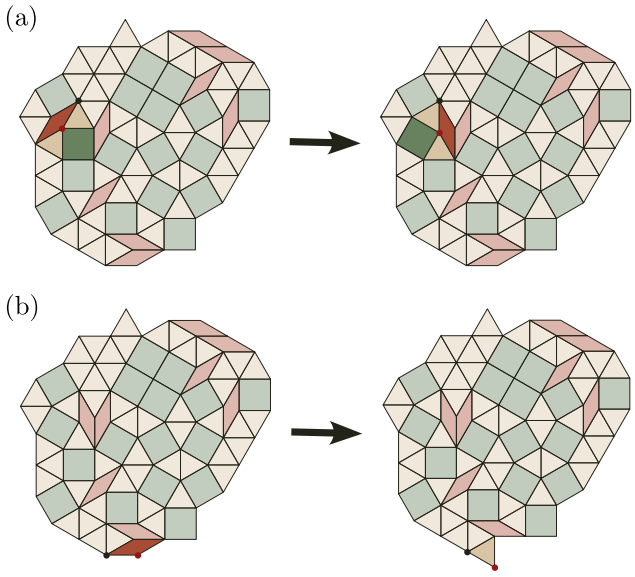

FIG. S3. Sample vertex moves in (a) bulk and at (b) the boundary.

this move, we focus on the pentagonal patches in the square-triangle-rhombus tiling. In our system there is only one allowed pentagonal patch, whose internal angles are $(\pi/3, 5\pi/6, \pi/2, \pi/2, 5\pi/6)$. As shown in Figure (S4), this pentagonal region has two different decompositions: (i) it can be decomposed into a square and a triangle, which we call the "house" configuration or (ii) it can be decomposed into two rhombi and a triangle, which we refer as the "R^2T" configuration.

After we identify these patches in the tiling, we perform the move by swapping a random pair of disjoint house and R^2T patches as seen in Fig(S5). Therefore, we implement the swap moves in three steps as:

1. Identify all house configurations in the tiling and randomly choose one.

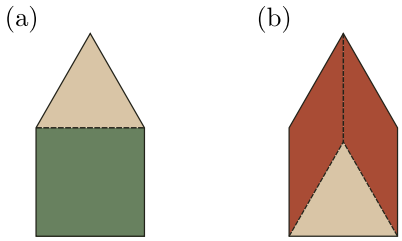

FIG. S4. The decompositions of the pentagonal patch: (a) the house configuration and (b) the R^2T configuration.

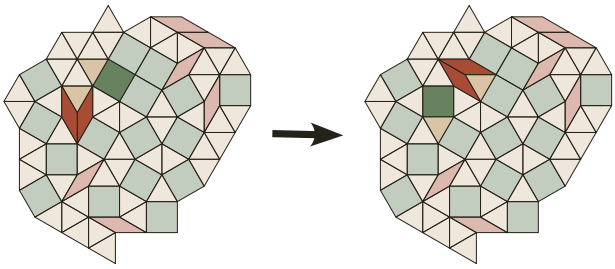

FIG. S5. An example of the swap move.

2. Identify all R^2T configurations in the tiling and randomly choose one.

3. If the chosen house and R^2T configurations are not disjoint, reject the move. Otherwise, accept the move and swap the configurations.

As the number of house and R^2T configurations do not change with swap moves, detailed balance is trivially satisfied. Moreover, since the swap moves do not change either the tile counts or the boundary length, they do not cause a potential energy change and are always accepted if they are valid. This results in a high acceptance rate. The non-local nature of the swap moves enables rapid rhombi propagation from boundary to bulk. This promotes local bulk rearrangements via vertex moves and speeds up the equilibriation process.

In the following subsection, we explain how we use the simulation results to calculate the configurational entropy of the square-triangle-rhombus tiling.

C. Configurational Entropy Calculation

To calculate the configurational entropy of the square-triangle-rhombus tiling, we first calculate the free energy of the tiling using thermodynamic integration with the pure square-triangle tiling as the reference state. Thus, the free energy of the square-triangle-rhombus tiling is given by

$$F(N,\gamma,T;\epsilon_R) = F_{\mathrm{sq-tr}}(N,\gamma,T) - \Delta F(N,\gamma,T;\epsilon_R) \tag{S13}$$

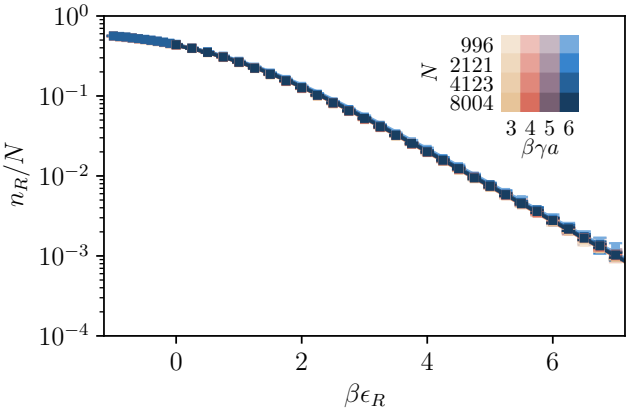

FIG. S6. The ensemble average of the number of rhombi with respect to varying rhombi biasing potential.

where the free energy difference $\Delta F(N,\gamma,T;\epsilon_R)$ is

$$\begin{aligned}\Delta F(N,\gamma,T;\epsilon_R) &= \int_{\epsilon_R}^{\infty} \mathrm{d}\epsilon_R' \frac{\mathrm{d}F(N,\gamma,T;\epsilon_R)}{\mathrm{d}\epsilon_R}, \\ &= \int_{\epsilon_R}^{\infty} \mathrm{d}\epsilon_R' \left\langle \frac{\mathrm{d}U}{\mathrm{d}\epsilon_R} \right\rangle_{N,\gamma,T,\epsilon_R'}, \\ &= k_BT \int_{\epsilon_R}^{\infty} \mathrm{d}\epsilon_R' \left\langle n_R \right\rangle_{N,\gamma,T,\epsilon_R'},\end{aligned} \tag{S14}$$

where $\langle \ldots \rangle$ represents an ensemble average. The free energy difference depends on the ensemble average of the number of rhombi, $\langle n_R \rangle_{N,\gamma,T,\epsilon_R'}$, in the tiling. Therefore, we need the functional form of this quantity to perform the thermodynamic integration.

The family of the functions that can describe the number of rhombi has three physical constraints that we need to impose: number of rhombi has to (i) decrease monotonically with increasing ϵ_R, (ii) approach N when $\epsilon_R \to -\infty$, and (iii) decay to 0 exponentially when as $\epsilon_R \to \infty$. When we impose these constraints and inspect our simulation results shown in Figure (S6), we see that the number of rhombi is well fitted by the function given by

$$\frac{\langle n_R \rangle_{N,\gamma,T,\epsilon_R}}{N} = \frac{1 + \nu_R e^{-\beta(\epsilon_R - \mu_R)/2}}{e^{\beta(\epsilon_R-\mu_R)} + \nu_R e^{-\beta(\epsilon_R-\mu_R)/2} + 2} \tag{S15}$$

where μ_R is the offset energy, and $\nu_R > 0$ is the shape parameter. Here, we observe the offset energy, and the shape parameter are parameters that depend on the system size and line tension listed in Table S2.

Then, we can obtain the closed form expression for the free energy difference by plugging Eq.(S15) into Eq.(S14)

N	$\beta\gamma a$	$\beta\mu_R$	ν_R	$\beta\mu_\rho$	ν_ρ	$\beta\mu_L$	ν_L	L_∞/Na	ω
996	3	0.06	0.42	-0.46	0.23	1.80	0.18	0.13	1.39
996	4	0.08	0.42	-0.44	0.23	1.68	0.20	0.12	1.39
996	5	0.11	0.42	-0.42	0.22	1.49	0.25	0.12	1.27
996	6	0.16	0.40	-0.36	0.20	1.32	0.31	0.12	1.17
2121	3	0.06	0.44	-0.48	0.23	1.96	0.13	0.09	1.72
2121	4	0.08	0.43	-0.47	0.22	1.70	0.19	0.08	1.41
2121	5	0.09	0.43	-0.45	0.21	1.47	0.23	0.08	1.33
2121	6	0.11	0.44	-0.44	0.22	0.86	0.42	0.08	0.97
4123	3	0.06	0.45	-0.49	0.21	1.67	0.20	0.07	1.26
4123	4	0.07	0.44	-0.49	0.21	1.63	0.19	0.06	1.34
4123	5	0.08	0.44	-0.47	0.20	1.33	0.26	0.06	1.17
4123	6	0.11	0.43	-0.45	0.19	0.69	0.43	0.06	0.97
8004	3	0.05	0.46	-0.52	0.26	1.74	0.18	0.05	1.29
8004	4	0.07	0.43	-0.51	0.23	1.17	0.28	0.04	1.13
8004	5	0.07	0.43	-0.50	0.22	1.10	0.32	0.04	1.12
8004	6	0.08	0.42	-0.49	0.22	1.69	0.18	0.04	1.46

TABLE S2. Fit parameters of Eqs.(S15, S19, S20) for the simulation data at different system sizes and line tensions.

and performing the integral. This yields,

$$\Delta F(N,\gamma,T;\epsilon_R) = -2Nk_BT\left[\sum_{k=1}^{3}\frac{(1+\nu_R z_k)\log(-z_k)}{4+3\nu_R z_k} - \sum_{k=1}^{3}\frac{(1+\nu_R z_k)\log\left(e^{-\beta(\epsilon_R-\mu_R)/2}-z_k\right)}{4+3\nu_R z_k}\right], \tag{S16}$$

where z_k are the three solutions of the following cubic equation,

$$\nu_R z_k^3 + 2z_k^2 + 1 = 0.$$

To calculate the entropy, we recall the fundamental identity, $F = U - TS$, relating the energy and the entropy to the free energy. Then, we can rewrite the free energy difference $\Delta F(N,\gamma,T;\epsilon_R)$ as

$$\begin{aligned}\Delta F(N,\gamma,T;\epsilon_R) &= \Delta U(N,\gamma,T;\epsilon_R) - T\Delta S(N;\epsilon_R),\\ &= \epsilon_R n_R(N,\gamma,T;\epsilon_R)\\ &\quad + \gamma\left[L(N,\gamma,T;\infty) - L(N,\gamma,T;\epsilon_R)\right]\\ &\quad - T\left[S_{\mathrm{sq-tr}} - S(N;\epsilon_R)\right],\end{aligned} \tag{S17}$$

where in the first line of the second step, we used $\epsilon_R n_R \to 0$ as $\epsilon_R \to \infty$. Furthermore, the configurational entropy of the square-triangle tiling per vertex is exactly calculated in the literature [4, 5] using Bethe ansatz to be

$$\frac{S_{\mathrm{sq-tr}}}{Nk_B} = \log(108) - 2\sqrt{3}\log\left(2+\sqrt{3}\right) = 0.12005524\ldots$$

Then, we can rearrange Eq.(S17) to obtain the configurational entropy of the square-triangle-rhombus tiling as

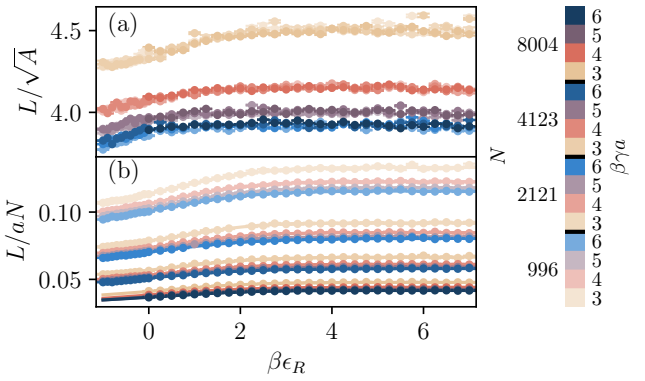

FIG. S7. The ensemble average of the boundary length with respect to varying rhombi biasing potential.

a function of the measurable quantities as

$$\begin{aligned}\frac{S(N;\epsilon_R)}{Nk_B} &= \frac{S_{\mathrm{sq-tr}}}{Nk_B} + \frac{\beta\epsilon_R}{N}\langle n_R\rangle_{N,\gamma,T,\epsilon_R}\\ &\quad + \frac{\beta\gamma}{N}\left[\langle L\rangle_{N,\gamma,T,\epsilon_R} - \langle L\rangle_{N,\gamma,T,\infty}\right]\\ &\quad - \frac{1}{N}\beta\Delta F(N,\gamma,T;\epsilon_R),\end{aligned} \tag{S18}$$

where $\langle n_R\rangle_{N,\gamma,T,\epsilon_R}$ and $\Delta F(N,\gamma,T;\epsilon_R)$ are given by Eq. (S15) and Eq. (S16) respectively. To calculate the configurational entropy from our simulations, we still need a function describing the behavior of the boundary length, $\langle L\rangle_{N,\gamma,T,\epsilon_R}$. Similar to the number of rhombi, the boundary length is also bounded from above and below. In particular, the bounds are given by

$$\sqrt{2\pi N} < L/a \leq 2N - 2,$$

where a is the tile edge length, the lower and the upper bounds are the circular rhombus tiling and linear chain limits, respectively. Upon inspection of our simulation data as seen in Figure S7, we observe that the boundary length follows a generalized logistic function given by

$$\langle L\rangle_{N,\gamma,T,\epsilon_R} = \sqrt{2\pi N} + \frac{L_\infty - \sqrt{2\pi N}}{\left(1+e^{-\omega\beta(\epsilon_R-\mu_L)}\right)^{\nu_L}}, \tag{S19}$$

where L_∞ is the boundary length at the square-triangle tiling limit, μ_L is the offset energy, $\nu_L > 0$ is the shape parameter, and $\omega > 0$ is the tail parameter. Similar to the number of rhombi, we observe that the fit parameters depend on the system size and line tension as listed in Table S2. Then, when we plug Eqs.(S15, S16, S19) into Eq.(S18), we get the configurational entropy per vertex parameterized by the rhombus biasing potential ϵ_R. Moreover, the size dependence, N, drops out in the infinite system limit since entropy per vertex is an intensive variable. Thus, we define the configurational entropy per vertex as

$$s(\epsilon_R) = \frac{S(N;\epsilon_R)}{N}.$$

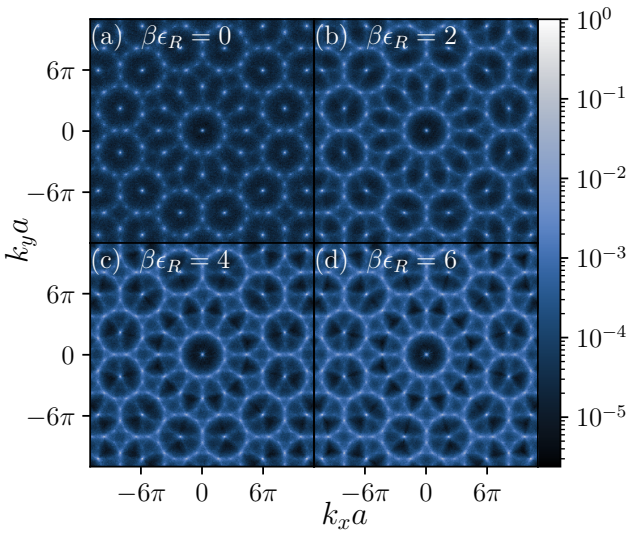

FIG. S8. 2D structure factors of single snapshots of the tilings at $N = 8004$, $\beta\gamma a = 4$, $\beta\epsilon_R =$ (a) 0, (b) 2, (c) 4, and (d) 6. The structure factors are Gaussian blurred with standard deviation $0.07/a$ to increase visibility.

Finally, we parameterize the area fraction of rhombi similar to n_R as

$$\langle\rho\rangle_{N,\gamma,T,\epsilon_R} = \frac{1 + \nu_\rho e^{-\beta(\epsilon_R - \mu_\rho)/2}}{e^{\beta(\epsilon_R - \mu_\rho)} + \nu_\rho e^{-\beta(\epsilon_R - \mu_\rho)/2} + 2}, \quad \text{(S20)}$$

where the fit parameters are listed in Table S2. Then the configurational entropy per vertex, $s(\rho)$, is fully characterized by Eq.(S18) and Eq.(S20).

III. 2D STRUCTURE FACTORS OF SINGLE SNAPSHOTS

Here we show that the 2D structure factors of single snapshots of the tiling remains consistent with 12-fold symmetry as seen in Fig S8.

IV. ALTERNATIVE REPRESENTATION OF THE PLOTS FROM FIGURE 2 A & C FROM THE MAIN TEXT

Due to the overlap of the curves in Fig. 2(a,c), we present them in an alternative way in Fig. S9 and Fig. S10 to improve clarity. Specifically, using $N_{\text{ref}} = 4123, \beta\gamma_{\text{ref}} a = 4$ as a reference point, we define the relative configurational entropy as $\delta S(N, \gamma, \epsilon_R) := S(N, \gamma, \epsilon_R) - S(N_{\text{ref}}, \gamma_{\text{ref}}, \epsilon_R)$. The corresponding relative configurational entropies are then plotted against the rhombus biasing potential (ϵ_R) and the rhombus area fraction (ρ).

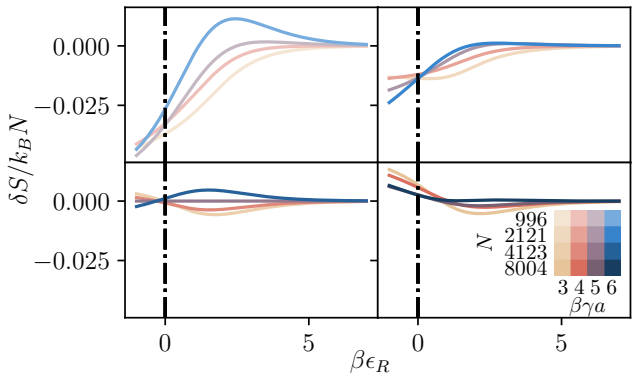

FIG. S9. Relative configurational entropy per vertex as a function of the rhombus biasing potential. Shown is the difference with respect to a reference system with $N_{\text{ref}} = 4123, \beta\gamma_{\text{ref}} a = 4$.

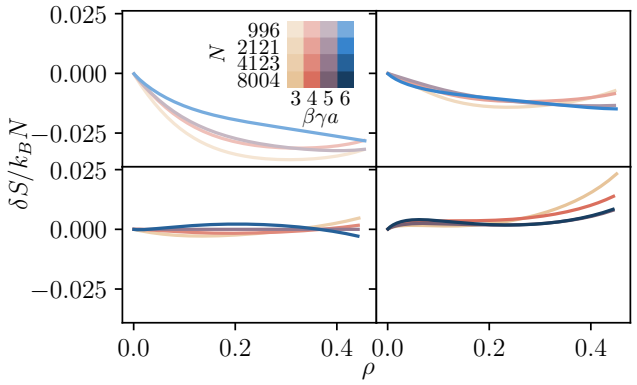

FIG. S10. Relative configurational entropy per vertex as a function of the rhombus area fraction. Shown is the difference with respect to a reference system with $N_{\text{ref}} = 4123, \beta\gamma_{\text{ref}} a = 4$.

V. MAPPING RHOMBI INTO SHIELDS AND EGGS

Since shield and egg tiles can each be decomposed into a square, two triangles, and a rhombus, as shown in Fig. S11, we can construct a map between square-triangle-rhombus tilings and square-triangle-shield-egg tilings in the limit where rhombi are sufficiently far away from each other.

To understand the mapping, we analyze the entropy contributions of configurations with a single rhombus tile and their corresponding shield-egg tilings. This mapping provides insights into the relationship between the entropy of rhombus defects and that of shield/egg defects.

When we start with a configuration containing exactly one rhombus, it can be mapped into a square-triangle-shield-egg tiling in two distinct ways by choosing which obtuse-angled vertex to take out. From local neighborhood mapping results shown in Fig. S12, we observe that,

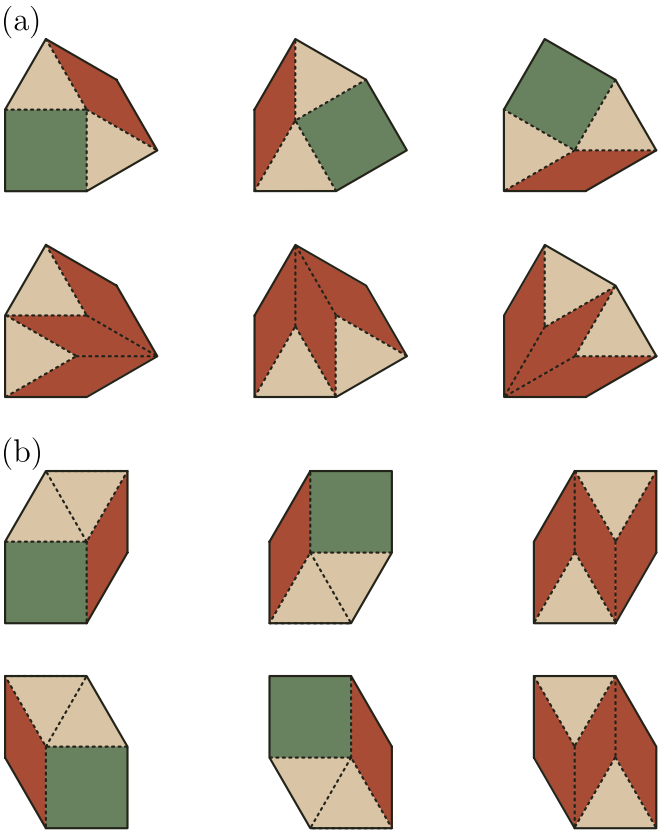

FIG. S11. Square-triangle-rhombus decorations of (a) the shield and (b) the egg tiles. In panel (b), the first row shows the decorations of left-handed egg and the second rows shows the right-handed egg.

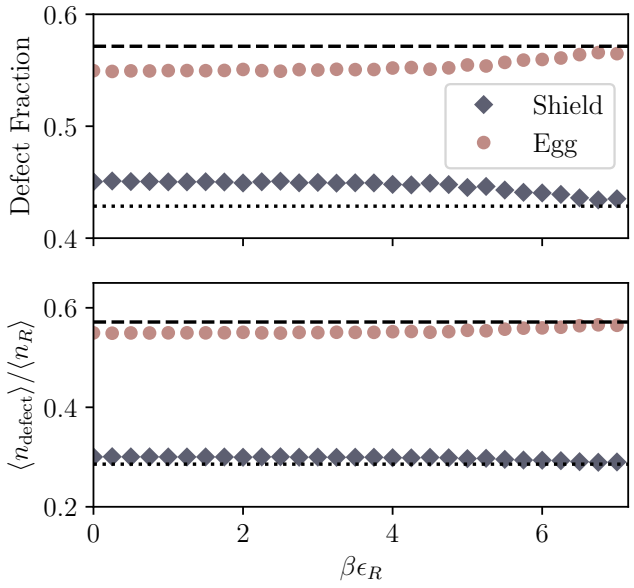

FIG. S12. Defect fraction and number of defects as a function of $\beta\epsilon_R$ for shields, eggs defects mapped from rhombi. In the upper panel, dashed and dotted lines correspond to the values 4/7 and 3/7, respectively. In the lower panel, dashed and dotted lines correspond to the values 4/7 and 2/7, respectively.

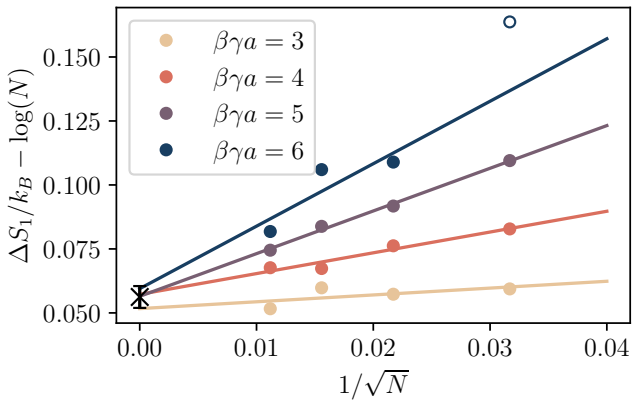

FIG. S13. Finite-size scaling of the configurational entropy difference, $\Delta S_1/k_B - \log(N)$, as a function of the inverse square root of number of vertices, for various line tensions $\beta\gamma a$. Linear fits demonstrate that the entropy converges to 0.056(4) (the $\times$ marker) in the thermodynamic limit ($1/\sqrt{N} \to 0$).

in the limit of low rhombus concentrations, we can map the rhombi to shields and eggs with the probabilities 3/7 and 4/7, respectively. However, due to the different decorations of the shield and egg tiles (i.e. the single-rhombus decorations shown in Fig. S11), shields are overcounted by a factor of 3, and eggs are overcounted by a factor of 2 in this mapping. To correct for this overcounting, we compute the number of distinct valid tilings that emerge from a single rhombus configuration.

For each rhombus, the average number of shield tiles generated is:

$$\frac{\langle n_{\text{Sh}}\rangle}{\langle n_R\rangle} = 2 \times \frac{1}{3} \times \frac{3}{7} = \frac{2}{7}$$

where the factors represent the choice of obtuse-angled vertex to take out, the overcounting-correction due to decorations and the mapping probability to a shield, respectively.

Similarly, the average number egg tiles is:

$$\frac{\langle n_{\text{Egg}}\rangle}{\langle n_R\rangle} = 2 \times \frac{1}{2} \times \frac{4}{7} = \frac{4}{7}$$

Thus, each tiling with a single rhombus generates an average of 6/7 tilings with either a shield or an egg, with eggs occurring twice as often as shields. This latter ratio can likely be attributed to the fact that egg tiles are chiral, and hence can occur in a left-handed or right-handed conformation, which cannot be mapped onto each other via rotation, as shown in Fig. S14(b). Hence, based on our measurements in Fig. S12, we predict that in the set of configurations with a single shield/egg defect, shields, left-handed eggs, and right-handed eggs all occur at the same frequency, and hence that these defect types have identical effects on the entropy of the tiling as long as they do not interact.

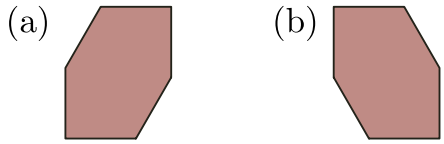

FIG. S14. Two chiralities of the egg tile: (a) left-handed egg, (b) right-handed egg.

As the transition from a rhombus to a shield or egg defect involved deleting a vertix, we finally have to replace the missing vertex. This placement contributes an additional entropy of $s_{\mathrm{Sq-Tr}} \approx 0.12 k_B$

Combining these factors, the entropy of a single shield/egg defect is related to the entropy of a single rhombus defect as follows:

$$\begin{aligned}\frac{\Delta S_{1,\mathrm{Sh/Egg}}}{k_B} &= \frac{\Delta S_{1,\mathrm{R}}}{k_B} + \log\left(\frac{6}{7}\right) + \frac{s_{\mathrm{Sq-Tr}}}{k_B} \\ &\approx 0.022 + \log N. \end{aligned} \tag{S21}$$

This is noticeably lower than the $\Delta S_{1,\mathrm{R}}/k_B \simeq 0.056 + \log N$ we found for a rhombus defect.

[1] M. Impéror-Clerc, A. Jagannathan, P. Kalugin, and J.-F. Sadoc, Square-triangle tilings: An infinite playground for soft matter, Soft Matter **17**, 9560 (2021).

[2] E. Fayen, M. Impéror-Clerc, L. Filion, G. Foffi, and F. Smallenburg, Self-assembly of dodecagonal and octagonal quasicrystals in hard spheres on a plane, Soft Matter **19**, 2654 (2023).

[3] M. Impéror-Clerc, P. Kalugin, S. Schenk, W. Widdra, and S. Förster, Higher-dimensional geometrical approach for the characterization of two-dimensional square-triangle-rhombus tilings, Phys. Rev. B **110**, 144106 (2024).

[4] M. Widom, Bethe ansatz solution of the square-triangle random tiling model, Phys. Rev. Lett. **70**, 2094 (1993).

[5] P. Kalugin, The square-triangle random-tiling model in the thermodynamic limit, J. Phys. A Math. Gen. **27**, 3599 (1994).